MICROGLIA AGING IN THE HIPPOCAMPUS ADVANCES THROUGH INTERMEDIATE STATES THAT DRIVE INFLAMMATORY ACTIVATION AND COGNITIVE DECLINE

Jeremy M. Shea[1]# and Saul A. Villeda[1-3]#

1. Department of Anatomy, University of California San Francisco, San Francisco, California 94143, USA
2. Department of Physical Therapy and Rehabilitation Science, University of California San Francisco, San Francisco, California 94143, USA
3. Bakar Aging Research Institute, University of California San Francisco, San Francisco, California, 94143, USA

#Corresponding Authors:

Dr. Saul Villeda, PhD
University of California San Francisco
Department of Anatomy
513 Parnassus Ave, Box 0452
San Francisco, CA 94143
Email: saul.villeda@ucsf.edu
Tel: 415-502-1929

Dr. Jeremy Shea, PhD
University of California San Francisco
Department of Anatomy
513 Parnassus Ave, Box 0452
San Francisco, CA 94143
Email: jeremy.shea@ucsf.edu
Tel: 617-460-4122

SUMMARY

During aging, microglia – the resident macrophages of the brain – exhibit dystrophic phenotypes and contribute to age-related neuroinflammation. While numerous hallmarks of age-related microglia dystrophy have been elucidated, the progression from homeostasis to dysfunction during the aging process remains unresolved. To bridge this gap in knowledge, we undertook complementary cellular and molecular analyses of microglia in the mouse hippocampus across the adult lifespan and in the experimental aging model of heterochronic parabiosis. Single-cell RNA-Seq and pseudotime analysis revealed age-related transcriptional heterogeneity in hippocampal microglia and identified intermediate states of microglial aging that also emerge following heterochronic parabiosis. We tested the functionality of intermediate stress response states via TGFβ1 and translational states using pharmacological approaches *in vitro* to reveal their modulation of the progression to an inflammatory state. Furthermore, we utilized single-cell RNA-Seq in conjunction with an *in vivo* adult microglia-specific *Tgfb1* conditional genetic knockout mouse model, to demonstrate that microglia advancement through intermediate aging states drives inflammatory activation and associated hippocampal-dependent cognitive decline.

INTRODUCTION

Microglia are one of few immune cells with long term residence in the brain parenchyma[1]. Microglia support neural development by synaptic pruning and neurogenic function in the developing brain, followed by homeostatic maintenance in the adult brain[2]. Alternatively, in the aged brain microglia exhibit dystrophic phenotypes, aggravating perceived insults rather than responding productively to environmental signals[3]. While microglia have been identified as principal mediators of multiple age-related neurodegenerative pathologies[4], mechanisms leading to microglia dysfunction during aging remain obscure.

Numerous studies have indicated that aged microglia are inflamed[5], have reduced phagocytic capacity[6,7], and have decreased motility[8]. Microglia exhibit several hallmarks of aging that potentially contribute to their age-related dysfunction, such as shortened telomeres[9], altered intercellular communication[10], molecular alterations[11], and a loss of proteostasis[12]. Furthermore, many recent studies have started to reveal the molecular changes that define microglial aging. Single cell RNA-Seq (scRNA-Seq) analyses indicate that microglia isolated from the entire brain lose homeostasis and activate inflammatory transcriptional profiles with age[13,14]. Data rich studies have also revealed partial overlaps between aging microglia and those from disease models, including Alzheimer's disease[15-19]. Interestingly, the microglial response to aging shows regional variation, as white matter-rich regions induce an interferon signature in aged microglia[20]. Studies using aged plasma administration and heterochronic blood exchange demonstrate that microglia aging is in part driven by the aged systemic environment [21,22]. However, the genesis of age-related dystrophic microglial phenotypes has not been extensively investigated. So, we set out to characterize the progression of age-related hippocampal microglial dysfunction, aiming to uncover intermediate states that could be intrinsic to the aging process. To do so, we undertook complementary cellular and molecular analyses of microglia across the adult lifespan and in heterochronic parabiosis - an experimental model of aging in which the circulatory systems of young adult and aged animals are joined[23].

In this study, we report that microglia in the adult mouse hippocampus, a brain region responsible for learning and memory and susceptible to age-related cognitive decline, advance through intermediate states that drive inflammatory activation during aging. We utilize scRNA-Seq across the adult lifespan to identify intermediate transcriptional states of microglial aging that emerge following exposure to an aged systemic environment. Functionally, we tested the role of these intermediate states using *in vitro* microglia approaches and an *in vivo* temporally controlled adult microglia-specific *Tgfb1* conditional genetic knockout mouse model to demonstrate that

118 intermediates represent checkpoints in the progression of microglia from homeostasis to
119 inflammatory activation, with functional implications for hippocampal-dependent cognitive decline.
120

121 **RESULTS**

122 **Single-cell transcriptional analysis reveals the dynamics of hippocampal microglia aging**

123 Previously, single-cell transcriptional profiling of microglia uncovered a diversity of responses
124 during development and in response to pathology aggregated over multiple brain
125 regions[13,14,16,19,24,25]. Microglia have region-specific transcriptional states, so we decided to focus
126 our analyses on the hippocampus[11], a region with well-reported functional differences during
127 aging[26]. Correspondingly, we investigated age-related transcriptional heterogeneity by performing
128 scRNA-Seq on hippocampal CD11b-positive cells isolated from mice at 6, 12, 18, and 24 months
129 of age using a commonly employed pooling strategy[18,27,28] (n = 1 pool of 5 biological replicates for
130 each age) to reveal the dynamics of microglia aging. 82% of cells isolated with CD11b were
131 identified as microglia using canonical markers with a small subset being proliferative (Figure
132 S1A-C). Dimensionality reduction revealed that non-proliferative microglia were grouped into
133 interconnected clusters that contained homeostatic, transition, and activated states, along with a
134 semi-distinct cluster with interferon activation (Figure 1a, S1D-G). Overlaying microglia ages onto
135 the clusters revealed progression from a homeostatic state in younger microglia to an activated
136 state in old microglia, suggesting that gradual transcriptional changes occur during microglial
137 aging (Figure 1B,C, S1H). Furthermore, the heterogeneity of microglial transcriptional programs
138 increased with age (Figure S1I). Expression of *Cx3cr1* and *Itgam* exemplified the homeostatic
139 state, while *B2m*, *Apoe*, *Cd48*, and *Lyz2* depict the activated state (Figure 1D). Interestingly,
140 several immediate early genes (*Jun*, *Klf2*, *Fos*), as well as the purinergic receptor gene *P2ry12*,
141 exhibited transient increases in expression at middle-age (Figure 1D). Alternatively, the interferon
142 cluster represents a small proportion of the overall microglia population with little age-related
143 changes in the number of these cells, but augmented expression of interferon genes during aging
144 (Figure 1A,C,D, S1G). Thus, gene expression changes exhibited unique patterns during aging,
145 with certain genes showing age-related decreases (e.g. *Tgfbr1*) or increases (e.g. *Apoe*), while a
146 subset of genes (e.g. *Tgfb1*) have peaks of expression at middle age (Figure 1D,E,G; Table S1).
147 Several complement genes implicated in age-related synaptic loss[10,29](e.g. *C1q* and *C3*)
148 demonstrated progressive age-related transcriptional increases, and the increased complement
149 activity in microglia was confirmed by immunohistochemistry (Figure 1E,F).

150 The effects of aging on microglia could be progressive or sudden, so we investigated if we
151 could find evidence of early aging of hippocampal microglia. We observe relatively few

differentially genes between 6- and 12-month (Figure 1G,H, Table S1). The number of differentially expressed genes gradually increased through the 24-month time point (Figure 1G-J, Table S1), suggesting that hippocampal microglia progressively accumulate aged-related expression changes. Furthermore, when investigating the outcome for genes with significant changes for each age, we find that genes that are differentially expressed at 12 months lose their expression change, while genes that change at later ages show progressive expression differences (Figure 1H). GO analysis of the microglia from 6- and 12-month-old mice revealed that activation and translational programs are modestly enriched in genes with increased expression during early aging (Figure 1I). The latter stages of aging display more prominent enrichment of immune activation and translation processes in genes with increased expression, while revealing that genes that regulate transcriptional processes exhibit decreased expression (Figure 1J,K). We corroborated the progressive increase in microglial activation by immunohistochemical analysis for CD68 and p65 (Figure S1J,K). Thus, microglia progressively age with subsets of cells at each age group being forerunners towards inflammatory activation or refractory to aging by remaining homeostatic. This analysis further suggests that microglia could pass through transitory states during aging.

Trajectory analysis indicates that aging microglia pass through intermediate states

To determine the transcriptional progression of microglia aging towards an inflammatory state, we performed pseudotime analysis of the scRNA-Seq data and observed several trajectories (Figure 2A). We find that the pseudotime trajectories progressed along the biological ages of the mice, indicating the suitability of this analysis for modeling aging progression in microglia (Figure 2B). We focus our analysis on one trajectory with two semi-distinct subbranches that terminated in inflammatory activation, since the alternate branch had minimal transcriptional differences between the beginning and end of the trajectory (Figure 2B,C). To gain insight into the transcriptional states of microglial aging along this inflammatory trajectory, we used spatial autocorrelation analysis and identified five expression modules of coregulated genes (Figure 2B,C, Table S2). We named these modules according to the most enriched GO pathways and known roles of prominent genes for microglia. This trajectory proceeds from high expression of homeostatic genes and mitochondrial processes (module 1) to transient expression of stress response genes and *Tgfb1* (module 2), of which TGFβ signaling is critical for microglia development[30]. A concerted increase in expression of ribosomal genes (module 3) precedes one subbranch of inflammatory activation (module 4), while the other myeloid activation subbranch (module 5), characterized by *B2m* and *C1qc* expression, proceeds independently of increased

186 ribosomal gene expression. GO analysis of genes specifically upregulated at 12-months showed
187 an enrichment of stress response pathways (Figure S2A,B), corroborating the findings of the
188 pseudotime analysis that intermediate stages of microglial aging pass through stress response
189 pathways. Thus, pseudotime trajectory analysis identifies a progression of intermediate states of
190 microglial aging with potential involvement in age-related maladaptive inflammation.

191 The gene level dynamics of microglia aging are further revealed when interrogating the
192 modules at each timepoint. Expression of several genes in the homeostatic cluster, including
193 *Cx3cr1* and *Tgfbr1*, progressively decline throughout the aging timeline (Figure 2D). Stress
194 response gene expression peaks at early timepoints during aging, while those genes in the
195 translation module have coherent upregulation at 24-months of age (Figure 2D). The top ranked
196 genes in the inflammation module gradually increase their expression throughout aging in a
197 consistent manner (Figure 2D). Alternatively, several genes in the myeloid activation module have
198 expression peaks at 12- (*Cst3*, *Selplg*) *or* 18-months (*Ctss*, *Cd9*) of age (Figure 2D). When the
199 modules are collapsed into metagenes, we observe that homeostatic module is reduced early on
200 in aging, while the stress response module follows later (Figure 2E-G). The ribosomal and
201 inflammatory modules display augmented expression at latter ages (Figure 2E-G). Alternatively,
202 the myeloid activation consistently has slightly increased expression throughout aging. These
203 results suggest that with advancing age microglia lose homeostatic and stress response
204 functions, while increasing their translational and inflammatory capacity.

205 Next, we utilized a publicly available scRNA-Seq datasets of pro-aging systemic
206 interventions and age-related neurodegenerative disease models to determine their impact on
207 hippocampal microglia aging trajectories. We used the heterochronic parabiosis model[31] to
208 investigate whether exposure to an aged systemic environment could promote progression of
209 young adult microglia along the identified aging trajectory (Figure 2H). First, using
210 immunohistochemistry for IBA1 and CD68, we reveal that an aged systemic environment
211 activates microglia (Figure S2C). Next, we find that hippocampal microglia from young adult
212 heterochronic parabionts have decreased expression of homeostatic genes (module 1), while
213 having increased expression of ribosomal genes (modules 3), inflammatory activation genes
214 (module 4) and myeloid activation genes (module 5) (Figure 2I, S2D). We used the $App^{NL\text{-}G\text{-}F}$
215 transgenic mouse model at 12 months of age to determine the effects of Alzheimer's disease
216 pathology on microglial aging[17] (Figure 2J). We observe exaggerated advancement along the
217 aging trajectory in $App^{NL\text{-}G\text{-}F}$ mice compared to controls, as expression is shifted towards the age-
218 associated modules (Figure 2K, S2E,F). These shift in gene expression posit that the aged

219 systemic and diseased environments drive adult microglia advancement along an aging-
220 associated inflammatory trajectory.
221
222 **Intermediate states of microglia aging act as checkpoints on inflammatory progression**
223 Next, we sought to corroborate microglial age-related molecular changes associated with
224 individual intermediate states in the aging hippocampus by RNAscope and immunohistochemical
225 analysis. Specifically, we assessed changes in the intermediate stress response (module 2) and
226 translation (module 3) modules by examining expression of *Tgfb1* (Figure 3A,B) and the ribosomal
227 protein S6 (Figure 3G,H), respectively. The vast majority (>95%) of *Tgfb1* signal localized to
228 microglia at every age (Figure S3A), indicating microglia are the predominant source for
229 hippocampal TGFB1. Consistent with scRNA-Seq data of aging microglia (Figure 1E), we
230 observed highest *Tgfb1* expression in microglia by middle-age (Figure 3B). TGFBR1 activation
231 was reduced during aging in hippocampal microglia (Figure S3B), and genes involved in the TGFβ
232 signaling pathway exhibited age-related expression changes with several having peak expression
233 at 12 months of age (Figure S3C). Additionally, we observed an increase in translational
234 components found during the scRNA-Seq analysis by immunohistochemistry for the ribosomal
235 protein S6 (Figure 3H)[32].
236 To complement hippocampal aging analysis, we assessed the impact of the aging
237 systemic milieu on both the TGFβ pathway and translational components in the young adult
238 hippocampus following heterochronic parabiosis. We observed a decrease in microglia *Tgfb1* and
239 TGFβ pathway expression in young adult heterochronic parabionts compared to age-matched
240 young adult isochronic controls[31] (Figure 3C, S3D). Additionally, expression of the translation
241 module in microglia increases following exposure to an aged systemic environment in the
242 heterochronic parabiosis model (Figure 3I).
243 To investigate the role of the intermediate stress response (module 2) and translation
244 (module 3) modules in mediating advancement through microglial activation states, we used an
245 *in vitro* approach. Primary microglia were treated with LPS, which induced gene expression
246 changes with a significant overlap to aging, as well as expression changes in aging modules
247 genes (Figure S3E,F; Table S3). We administered TGFB1 to activate TGFβ signaling (module 2)
248 (Figure 3A) and CX-5461 to inhibit RNA Pol I synthesis and interfere with translation (module 3)
249 (Figure 3G) in the context of microglial activation. TGFB1 treatment modified the transcriptional
250 states of LPS-treated microglia (Figure S3G) and caused decreased expression of inflammatory
251 immune processes after LPS stimulation (Figure 3D). TGFB1 treatment reduced expression of
252 later aging modules (modules 2, 3 and 4) and restored expression of the homeostatic gene *Cx3cr1*

253 (Figure 3E,F), suggesting that TGFBβ signaling acts as an aging checkpoint during microglial
254 stress response. Targeting translation (module 3) with CX-5461 attenuated expression of immune
255 processes after LPS stimulation (Figure 3J; Table S3), as well as decreased expression of genes
256 in modules 2, 3, and 4, while restoring expression of homeostatic genes in module 1 (Figure
257 3K,L). Interestingly, CX-5461 treatment had no effect on genes in module 5, which is located on
258 an independent myeloid activation trajectory from altered translational gene expression (Figure
259 3K,L). These *in vitro* perturbation data identify active roles for intermediate states in mediating
260 advancement along aging-associated inflammatory trajectories.
261
262 **Mimicking age-related changes in microglia-derived TGFB1 promotes microglial**
263 **advancement along an aging-associated inflammatory trajectory *in vivo***
264 Having uncovered roles for intermediate states in advancing microglia along aging-associated
265 inflammatory trajectories *in vitro*, we next investigated the role of individual aging modules in adult
266 microglia *in vivo*. We elected to disrupt the transition from homeostasis to inflammatory activation
267 by targeting microglia-derived TGFB1, a key marker of the stress response intermediate state
268 (module 2). While TGFB1 is critical for microglia development[33], the role of microglia-derived
269 TGFB1 in regulating microglia homeostasis during aging remains to be defined.
270 We generated *Tgfb1*$^{flox/flox}$, *Tgfb1*$^{flox/wt}$, and *Tgfb1*$^{wt/wt}$ mice carrying an inducible *Cx3cr1-*
271 *Cre-ER* gene, in which *Tgfb1* is excised specifically in adult microglia upon tamoxifen
272 administration (*Tgfb1* cKO, *Tgfb1* Het, and WT, respectively) (Figure 4A). To disrupt the age-
273 related increase in microglia *Tgfb1* observed between mature and middle-age (Figure 1E and
274 Figure 3B), mature adult mice were administered tamoxifen and molecular changes were
275 assessed two months later (Figure 4A). We find that microglia activation, as measured by
276 CD68/IBA1 immunohistochemistry, exhibited genotype-dependent effects (Figure S4A). We
277 performed scRNA-Seq on microglia isolated from WT, *Tgfb1* Het and *Tgfb1* cKO mature mice (n
278 = 2 pools of 3 animals per genotype), and detected genotype-dependent changes in
279 *Tgfb1*expression levels, as well as effectors of TGFB1 signaling (Figure S4B). Dimensionality
280 reduction and clustering of cells from scRNA-Seq revealed readily identifiable clusters based on
281 marker expression (Figure 4B). Composition of these clusters were dependent on the microglia
282 genotype, with WT microglia representing the largest fraction of the homeostatic cluster and *Tgfb1*
283 cKO microglia representing the largest fraction of the activated cluster (Figure 4C, S4C). Next,
284 we assessed whether deletion of *Tgfb1* in mature adult microglia impacted advancement along
285 aging-associated inflammatory trajectories. Interestingly, when we analyze the effects of *Tgfb1*
286 dosage on the aging modules, we find that the loss of a single *Tgfb1* allele reduces expression of

287 homeostatic genes (module 1), while increasing expression of translation-related genes (module
288 3) (Figure 4D,E). In addition to a decrease in expression of homeostatic genes (module 1), loss
289 of both *Tgfb1* alleles caused a greater increase in expression of translation-related genes (module
290 3), and led to a profound increase in inflammatory activation genes (module 4) (Figure 4D,F).
291 Results were corroborated in an independent cohort of mature *Tgfb1* cKO mice, in which we
292 detected altered levels of immune- and age-related cell surface markers (Figure S4D,E),
293 transcriptional alterations that significantly overlapped with aging (Figure S4F-H; Table S4), and
294 progression along the aging-associated inflammatory trajectories (Figure S4I,J). These data
295 indicate that microglia-derived TGFB1 is both necessary for expression of youth-associated
296 homeostatic genes and prevents aberrant microglia inflammatory activation, further suggesting
297 that TGFBβ signaling acts as a checkpoint in mediating advancement along aging-associated
298 inflammatory trajectories.
299
300 **Mimicking age-related changes in microglia-derived TGFB1 impairs hippocampal-**
301 **dependent cognitive function**
302 It is becoming increasingly apparent that microglia interact with other cell types in the brain to
303 influence cognitive function[2,34]. Given loss of microglia-derived TGFB1 promoted microglia
304 progression along aging-associated inflammatory trajectories, we next investigated its functional
305 consequence on cognition. We assessed hippocampal-dependent learning and memory in WT,
306 *Tgfb1* Het and *Tgfb1* cKO mature mice using novel object recognition and contextual fear
307 conditioning - behavioral paradigms that are sensitive to age-related impairments[35,36]. During
308 novel object recognition testing, WT mice were biased toward a novel object relative to a familiar
309 object while neither *Tgfb1* Het or *Tgfb1* cKO mice showed any preference (Figure 4G). During
310 contextual fear conditioning testing, *Tgfb1* Het and *Tgfb1* cKO mice exhibited less freezing
311 compared to WT controls (Figure 4H). Alternatively, we assessed amygdala-dependent fear
312 memory by cued fear conditioning (Figure S4K)[37] and short-term spatial reference memory by Y
313 maze (Figure S4L)[38], and observed no differences across genotypes. As a control, we also
314 profiled general health using an open field paradigm and observed no differences in total distance
315 traveled or time spent in the center of the open field, indicative of normal motor and anxiety
316 functions (Figure S4M). These behavioral data indicate that loss of microglia-derived TGFB1 not
317 only impacts aging-associated inflammatory trajectories but also promote hippocampal-
318 dependent cognitive impairments characteristic of age-related functional decline.
319
320 **DISCUSSION**

Cumulatively, we demonstrate that microglia aging in the hippocampus advances through intermediate states that precede inflammatory activation, with functional implications for age-related cognitive decline. These transient states, such as activation of the stress response and TGFβ signaling, act as checkpoints on further age-related activation. Furthermore, microglia asynchronously progress through this inflammatory aging trajectory that is in turn influenced by the systemic environment and neurodegenerative disease states.

Analysis of our scRNA-Seq data elucidate cryptic, but necessary, intermediate states of microglia progression to age-related inflammatory activation. These states are present in middle-aged mice and constitute stress response pathways likely responsive to internal and external cellular insults[39,40]. Pseudotime analysis suggests a highly plausible sequence of molecular alterations that lead to age-related inflammatory activation of hippocampal microglia. First, mitochondrial dysfunction triggers a stress response, and products of this stress response (e.g. TGFB1) attempt to return microglia to homeostasis[41]. Here, chronic activation of the stress response leads to subsequent increased translational capacity that promotes inflammatory activation[42]. Alternatively, another branch of microglial activation advances independently of increased translational capacity, evidenced by translational inhibition having little effect on its activation following LPS stimulation. Thus, we find that increases in translational capacity predicate age-related inflammatory phenotypes, identifying potential targets to counter microglial aging. Analysis of scRNA-Seq data further identify intermediate states of microglial aging in young adult heterochronic parabionts, suggesting a pivotal role for the aged systemic environment in driving advancement towards age-related inflammatory activation.

While we find evidence of the beginnings of inflammatory activation in the hippocampus by middle age (12 months), consistent with the timing recently reported in the whole brain[14], it should be noted that scRNA-Seq analysis of the whole brain did not observe intermediate stages in microglial aging[14]. These disparate observations could likely be the result of analyzing multiple regions with highly differentiated transcriptional programs[11] that could obfuscate regional aging trajectories. This further underscores the need for both temporal and regional specificity in aging studies, given the level of cellular heterogeneity observed across ages and brain regions. Moreover, studying microglia - or other cell types - at early stages of aging in a region-specific manner could also represent useful models to investigate the ontogeny of aging without the confounding effects of accumulated functional deficits.

Of note, we find that an inflammatory trajectory of microglia aging can be mitigated *in vitro* by environmental TGFβ signaling, while loss of microglia-derived TGFB1 promoted progression along aging-associated inflammatory trajectories *in vivo*. Together, these data indicate that TGFβ

signaling is necessary for maintaining youth-associated homeostasis and represents a checkpoint in mediating advancement along aging-associated inflammatory trajectories. Functionally, loss of microglia-derived TGFB1 resulted in hippocampal-dependent cognitive impairments, suggesting that advancement through aging-associated inflammatory trajectories may facilitate age-related cognitive decline. TGFβ likely acts in an autocrine fashion to return microglia to a homeostatic state after encountering stressful stimuli. Given that a transient increase in *Tgfb1* expression is observed in middle-aged microglia, it is possible that maintaining stress response-mediated signaling into older ages may also provide a means to delay age-related microglial dysfunction and maintain cognitive function. Alternatively, TGFβ signaling impairs microglial responses to Alzheimer's disease pathology[43], suggesting that the dynamic regulation of TGFβ signaling in response to aging-associated pathologies is necessary for tuning microglial responses.

While microglia have been demonstrated to mediate the establishment of cognitive function during development[2] and play prominent roles in neurodegeneration[44], little is known about how age-related changes in microglia affect cognitive function. The specificity of the cognitive deficits that we observe in *Tgfb1* Het and *Tgfb1* cKO mice suggests that age-related changes in microglia-derived TGFB1 predominantly impacts hippocampal-dependent cognitive decline. Furthermore, the deficits observed in *Tgfb1* heterozygous mice point to the importance of maintaining youthful levels of microglia-derived TGFB1 to counteract stressors that accrue during aging.

Altogether, our results highlight the need to investigate aging across the lifespan in a region-specific manner to reveal necessary cellular intermediates in the aging process. While the present study focuses on age-related changes in microglia, our findings have broad implications for other studies in determining the extent to which aging sequelae are conserved across different cell types in the hippocampus. Furthermore, therapeutic interventions targeting intermediate states in the aging process hold far reaching potential to counteract the development of age-related pathologies, including those promoting cognitive dysfunction.

ACKNOWLEDGMENTS

We thank Dr. Erik Ullian for critically reading manuscript. **Funding**: This work was funded by National Institute on Aging (AG055292 (J.M.S.), AG055797 (S.A.V.), AG077816 (S.A.V.)), Simons Foundation (S.A.V). The authors declare no competing financial interests.

AUTHOR CONTRIBUTIONS

J.M.S and S.A.V. developed concept and designed experiments. J.M.S conducted experiments, collected data, and performed analysis. J.M.S and S.A.V wrote manuscript. S.A.V supervised all aspects of the project. All authors had the opportunity to discuss results and comment on manuscript.

COMPETING INTEREST STATEMENT

The authors declare no competing interests.

Fig. 1 | Hippocampal microglia exhibit progressive age-related transcriptional inflammatory activation. A, UMAP plot of microglia separated into transcriptional clusters. (n = 1 pool of 5 animals for each age) **B,** Superimposition of ages onto the UMAP plot with dashed lines signifying relative cluster demarcation. **C,** Percent composition of each cluster by age. **D,** Dot plot of expression of cluster markers sorted by age. Percent of cells expressing the gene and average normalized expression are represented. **E,** Violin plots of genes with dynamic age-related expression patterns. **F,** Representative images and quantification of C1q (yellow), C3 (red), and Iba1 (cyan) staining in the hilus and molecular layer (ML) of 6- and 24-month-old mice. (n=4-5 mice per group; mixed effects analysis followed by Dunnett's multiple comparisons; *P<0.05, **P<0.01, ****P<0.0001). **G,** Number of differentially expressed genes from the 6-month timepoint at each age. Bars above the intersect represent increased expression and those below represent decreased expression. **H,** The average expression change at all ages for genes differentially regulated genes at individual ages represented by the color scheme in **B**. **I, J, K,** Volcano plots of differentially expressed genes in microglia between 6- and 12-months (**I**), 6- and 18-months (**J**), and 6- and 24-months (**K**) and corresponding gene ontology analysis of genes with significantly increased (brown) or decreased (green) expression for each comparison. Data are shown as mean±s.e.m.

Fig. 2 | Hippocampal microglia aging advances through intermediate states that respond to systemic interventions or disease states. A, Pseudotime trajectories of microglia from an anchor point located in 6-month microglia presented in a UMAP plot. (n = 1 pool of 5 animals for each age) **B,** Microglia ages superimposed over pseudotime trajectories. **C,** Gene expression modules representing sections of the inflammatory aging trajectory over the right half of the UMAP plot (left). Modules were discovered using Moran's I autocorrelation test. Top Gene Ontology terms and representative genes in each module (right). **D,** Dotplot of pseudotime modules sorted by age. Percent of cells expressing the gene and average normalized expression are represented. **E, F, G,** Average gene expression changes for each aging module represented as log2 fold change of 12-months (**E**), 18-months (**F**), or 24-months (**G**) over 6-months. **H,** Diagram of the heterochronic parabiosis model with the comparisons made in scRNA-Seq. **I,** Average gene expression changes for each aging module represented as log2 fold change of heterochronic young (HY) over isochronic young (IY) adult parabionts. Data from [31]. **J,** Diagram of microglia surrounding an Aβ plaque. **K,** Average gene expression changes for each aging module represented as log2 fold change of the $App^{NL\text{-}G\text{-}F}$ genotype (AD) over wildtype (WT). Data from[17]. (one sample T-test with the expected value of 0 (no change); *P<0.05, **P<0.01, ***P<0.001, ****P<0.0001).

Fig. 3 | Intermediate states of microglia aging act as checkpoints on inflammatory progression. A, Representation of the microglia aging trajectory over the UMAP plot highlighting the region of peak *Tgfb1* expression. **B,** Representative RNAscope images and quantification of *Tgfb1* (red) expression in IBA1 (cyan) cells across ages. (n=5 per group; one-way ANOVA with Dunnett's post-hoc test; *P<0.05, **P<0.01)**. C,** Schematic of the heterochronic parabiosis model and quantification of hippocampal microglia expression of *Tgfb1* from isochronic young (IY) and heterochronic young (HY) adult parabionts. Data derived from Pálovics *et al*[31]. **D,** Top gene ontology terms of genes with significantly decreased expression in bulk microglia RNA-Seq following TGFB1 treatment compared to control (DMSO) in LPS treated microglia. (n=5 per group) **E,** Heatmap of top 10 genes in each aging module following TGFB1 compared to DMSO in LPS treated microglia. **F,** Average gene expression changes for each aging module represented as log2 fold change of TGFB1 treatment over DMSO. (one sample T-test with the expected value of 0 (no change); *P<0.05, ***P<0.001, ****P<0.0001). **G,** Representation of the microglia aging trajectory over the UMAP plot highlighting the stage where CX-5461 modulates the trajectory. **H,** Representative images of S6 (magenta) and Iba1 (cyan) staining in the hippocampus of 6- and 24-month-old mice and quantification across aging. (n=3 mice per group; one-way ANOVA with Tukey's post hoc test; *P<0.05, **P<0.005, ****P<0.0001). **I,** Schematic of the heterochronic parabiosis model and quantification of hippocampal microglia expression of translation module from isochronic young (IY) and heterochronic young (HY) adult parabionts. Data derived from Pálovics *et al*[31]. (one sample T-test with the expected value of 0 (no change); **P<0.01). **J,** Top gene ontology terms of genes with significantly decreased expression in bulk microglia RNA-Seq following CX-5461 treatment compared to control (DMSO) in LPS treated microglia. (n=3 per group) **K,** Heatmap of top 10 genes in each aging module following CX-5461 compared to DMSO in LPS treated microglia. **L,** Average gene expression changes for each aging module represented as log2 fold change of CX-5461 treatment over DMSO. (one sample T-test with the expected value of 0 (no change); *P<0.05, **P<0.01, ****P<0.0001).

Fig. 4 | Targeting age-related changes in microglia-derived TGFB1 promotes microglia advancement along inflammatory trajectories in the hippocampus and impairs cognition. **A,** Schematic of *in vivo* manipulation schema of Module 2. Adult (7-8 months) littermate *Cx3cr1-Cre-ER*$^{+/wt}$; *Tgfb1*$^{flox/flox}$ (cKO), *Cx3cr1-Cre-ER*$^{+/wt}$; *Tgfb1*$^{flow/wt}$ (Het), and *Cx3cr1-Cre-ER*$^{+/wt}$; *Tgfb1*$^{wt/wt}$ (WT) mice were administered tamoxifen and subject to hippocampal microglia scRNA-Seq and behavior analysis two months later. **B,** UMAP plot of microglia separated into transcriptional clusters. (n = 2 pools of 3 animals per genotype) **C,** Stacked bar plot of the normalized relative percentage of cells of each genotype in the identified clusters. **D,** Dot plot of expression of aging module markers sorted by genotype. Percent of cells expressing the gene and average normalized expression are represented. **E,F,** Average gene expression changes for each aging module represented as log2 fold change of either Het over WT (**E**) or KO over WT (**F**). (one sample T-test with the expected value of 0 (no change); *P<0.05, ****P<0.0001)**. G,** Novel object recognition task. (Top) Diagram of the training and testing phases of the novel object recognition paradigm. (Bottom) Quantification of the NOR testing phase represented as percentage of time spent with the novel object (over the total time spent interacting with the objects). (n=9-13 per genotype; one sample T-test with the expected value of 50 (equal time spent with each object); ***P<0.001)(differences between groups determined by one-way ANOVA; **P<0.01)**. H,** Contextual fear conditioning. (Top) Diagram of the fear conditioning paradigm. (Bottom) Quantification of the percentage of time mice froze in the contextual fear conditioning testing phase. (n=14-16 per genotype; one-way ANOVA; *P<0.05). Data are shown as mean±s.e.m.

627 **METHODS**

628 **Mice**

629 All animal procedures were performed in accordance with protocols approved by the UCSF
630 IACUC. Animals were housed in SPF barrier facilities and provided continuous food and water
631 along with environmental enrichment. Aging characterizations were performed on an inhouse
632 C57BL/6J mouse colony where 2-month-old mice were purchased from Jackson Laboratories
633 (Stock 000664) and aged in the UCSF Parnassus barrier facility. Timed pregnant females were
634 obtained for isolation of primary microglia from newborn pups. Male mice were used in all
635 experiments. B6.129P2(Cg)-*Cx3cr1*$^{tm2.1(cre/ERT2)Litt}$/WganJ (*Cx3cr1*Cre^{ER}) (Stock 021160) and
636 C57BL/6J-Tgfb1^{em2Lutzy}/Mmjax (*Tgfb1*-flox) (Stock 65809-JAX) mice were obtained from Jackson
637 Laboratories. Mice were bred to obtain *Cx3cr1*Cre^{ER} +/wt with either *Tgfb1* wt/wt, *Tgfb1* fl/fl. As
638 *Cx3cr1*Cre^{ER} is a knock-in/knock-out allele for the microglia homeostatic gene *Cx3cr1*, all mice
639 tested were *Cx3cr1*Cre^{ER} +/wt. To induce recombination and deletion of *Tgfb1* by Cre^{ER}, we
640 injected tamoxifen for 5 days at 90mg/kg daily, and mice were analyzed after 60 days.

641

642 **Parabiosis**

643 Parabiosis surgery followed previously described procedures[45]. Mirror-image skin incisions at the
644 left and right flanks were made through the skin, and shorter incisions were made through the
645 peritoneum. The peritoneal openings of the adjacent parabionts were sutured together with
646 chromic gut suture (MYCO Medical, GC635-BRC). Apposing elbow and knee joints from each
647 parabiont were sutured together (Coated VICRYL Suture, Ethicon, J386) and the skin of each
648 mouse was stapled (9-mm Autoclip, Clay Adams, 427631) to the skin of the adjacent parabiont.
649 Each mouse was injected subcutaneously with Carpofen, Enrofloxacin, and Buprenex as directed
650 for pain and monitored during recovery. For overall health and maintenance behavior, several
651 recovery characteristics were analyzed at various times after surgery, including pair weights and
652 grooming behavior.

653

654 **Bulk Microglia RNA-Seq**

655 Microglia were isolated from C57BL6/J, *Tgfb1* cHet, and *Tgfb1* cKO using FACS. Briefly, mice
656 were sedated with ketamine followed by perfusion with 30mL of ice-cold PBS. The entire brain
657 was removed, then the hippocampus was sub-dissected. Single-cell suspensions were generated
658 by enzyme-mediated (papain) and mechanical dissociation using Miltenyi Neural Dissociation Kits
659 (P) (Miltenyi, 130-092-628) according to the manufacturer's instructions. Myelin was depleted
660 from the suspensions using Myelin Removal Beads (Miltenyi, 130-096-731). Cells were labeled

661 with CD11b-APC (eBioscience, 17-0112-82, RRID:AB_469343) and CD45-PE (eBioscience, 12-
662 0451-82, RRID:AB_465668), then sorted at 4°C into Tri Reagent with a FACS AriaII (BD). The
663 gating strategy for microglia isolation is presented in Figure S1D, showing the collection of
664 $Cd11b^{+}Cd45^{Intermediate}$ cells. During the collection of control and *Tgfb1* microglia, CD48 was
665 detected in $Cd11b^{+}Cd45^{Intermediate}$ cells using CD48-Pacific Blue (BioLegend, 103417,
666 RRID:AB_756139). FlowJo was used to analyze flow cytometry data. RNA was isolated from
667 microglia using Tri Reagent (Sigma-Aldrich, T9424). RNA pellets were resuspended in 5uL TE
668 buffer.
669
670 RNA was transformed into RNA-Seq libraries using an adapted version of the Smart-Seq2
671 protocol[46]. Briefly, 5ng of total RNA was reverse transcribed with SuperScript II (Thermo Fisher,
672 18064014) supplemented with betaine and $MgCl_2$ using an oligo-dT RT primer
673 (AAGCAGTGGTATCAACGCAGAGTACT(30)VN) with a PCR binding site and a template
674 switching oligonucleotide (5′ AAGCAGTGGTATCAACGCAGAGTACATrGrG+G) with a
675 homotypic PCR binding site. Betaine and MgCl2 were added to enhance the reaction. After
676 reverse transcription, whole transcriptome amplification by PCR was performed for 12 cycles
677 using KAPA HiFi HotStart ReadyMix (Roche, 7958935001) with a PCR primer
678 (AAGCAGTGGTATCAACGCAGAGT). The PCR reaction was cleaned up with Ampure XP beads
679 (Beckman Coulter, A63881). In addition, after the whole transcriptome PCR amplification step,
680 qPCR was performed to determine the presence of microglia-specific transcripts (*Cx3cr1*) and
681 housekeeping genes (*Gapdh*). The amplified DNA was diluted to a concentration of 0.5ng/ul, and
682 subjected to tagmentation with the Illumina Nextera XT kit (Illumina, FC-131-1096). Each sample
683 was PCR amplified with a unique set of Nextera indices. Bulk microglia RNA-Seq libraries were
684 sequenced on an Illumina HiSeq, while *in vitro* microglia RNA-Seq libraries were sequenced on
685 an Illumina Nova-Seq.
686
687 **RNA-Seq Analysis**
688 FASTQ reads were pseudo aligned to the mouse transcriptome (GRCm39 cDNA from Ensembl)
689 using kallisto[47] with default parameters. Next, transcript abundance estimates were imported into
690 DeSeq2[48]. Differential expression analysis was performed using DeSeq2 using the Wald
691 significance test. Gene ontology analysis was performed with Panther[49-51]. Principal component
692 analysis plots were generated with the plotPCA function included with DeSeq2 and graphed with
693 ggplot2. Heatmaps were generated with the pheatmap package in R.

694 The overlap between gene expression differences in aging and LPS treatment were
695 determined using genes significantly changed between the 6- and 24-month-old timepoints in the
696 scRNA-Seq data and the control and LPS treated primary microglia. χ^2 test was used to determine
697 the significance of the overlap between these two datasets. The Venn diagram was generated
698 using the VennDiagram package in R.
699
700 **10x Genomics Single Cell RNA-Sequencing**
701 10x Single-Cell RNA-Seq libraries were generated from Cd11b+ cells isolated from the
702 hippocampi of an aging cohort of mice consisting of 6-, 12-, 18-, and 24-month-old C57BL/6J mice
703 that were all collected and processed on the same day in an interspersed order. Mice were
704 sedated with ketamine followed by perfusion with ice-cold PBS. Subsequently, the entire brain
705 was removed from the mouse followed by sub-dissection of the hippocampus. For each age,
706 hippocampi from five mice were pooled during the dissection step in HBSS at 4°C. Single-cell
707 suspensions were generated by enzyme-mediated (papain) and mechanical dissociation using
708 Miltenyi Neural Dissociation Kits (P). The papain dissociation was done at 37°C for 10 minutes
709 with 3 trituration steps. All other processing steps were performed at 4°C. Myelin was depleted
710 from the suspensions using Myelin Removal Beads (Miltenyi). Microglia were enriched using
711 Cd11b magnetic beads (Miltenyi, 130-126-725). Cell viability was determined to be over 95%.
712 Single-cell RNA-Seq 3' libraries were generated from the cell suspension using 10x Genomics
713 Chromium Single-Cell 3' Solution. Libraries were sequenced on the Illumina Nova-Seq. Cell
714 Ranger demultiplexed and mapped (using bcl2fastq) reads, followed by alignment (with STAR),
715 and generation of single-cell expression matrices[52].
716 The isolation protocol for the *Tgfb1* genetic mouse model was modified. We added
717 transcriptional and translational inhibitors (Actinomycin D (Sigma-Aldrich, A1410), Anisomycin
718 (Sigma-Aldrich, A9789), and Triptolide (Sigma-Aldrich, T3652) to prevent transcriptional changes
719 due to *ex vivo* activation [53]. We utilized the concentrations presented in Marsh *et al*. 2022[53].
720
721 **Single-cell RNA-Seq Analysis**
722 Seurat: The single-cell gene expression matrices generated by Cell Ranger were loaded into
723 Seurat[54].
724
725 Aging microglia dataset. Cells were filtered according to the following parameters: Genes > 1000
726 & RNA count > 10000 & mitochondrial percentage < 5. The count data was log normalized. The
727 2,500 most variable genes were identified using the "vst" method. The expression data was scaled

728 and centered. Principal component analysis was performed, and the first 25 PCAs were used to
729 identify nearest neighbors, and interconnected clusters were identified with a resolution of 0.4.
730 UMAP was used to visualize the results. Preliminary dimensionality reduction and visualization
731 with UMAP using 25 PCAs and 25 nearest neighbors in Seurat identified a large microglia cluster,
732 plus sparse clusters consisting of astrocytes, vascular cells, neutrophils, and macrophages. *Hexb*,
733 *P2ry12*, *Tmem119*, and *Slc2a5* are used as markers to identify microglia in the preliminary
734 clustering, while *Nrxn1* (neurons), *Tm4sf1* (vasculature), *Dclk*1 (astrocytes), *Sdpr* (vasculature
735 smooth muscle), *Abcb1a* (pericyte/vasculature), and *Foxq1* (macrophages) identified other cell
736 types. The data was then subsetted on the non-proliferating microglial clusters (to avoid
737 confounds associated with the cell cycle). The top 1,500 most variable genes in the subsetted
738 microglia were identified using the "vst" method. The data was scaled and centered. Principal
739 component analysis was performed, and the first 8 PCAs were used to identify nearest neighbors,
740 and interconnected clusters were identified with a resolution of 0.25. UMAP was used to visualize
741 the results using 8 PCAs and 100 nearest neighbors. Gene enrichment and differential expression
742 analysis was performed on the filtered dataset to determine differences between ages.
743
744 *Tgfb1* cKO microglia dataset. Cells were prefiltered according to the following parameters: Hexb
745 > 4 & Tmem119 > 1 & Cx3cr1 > 4 & Top2a < 1 & Mki67 < 1 nFeature_RNA > 1000 &
746 nFeature_RNA < 6000 & nCount_RNA > 2000 & nCount_RNA < 40000 & percent.mt <10. Data
747 was integrated using IntegrateData and scaled. Principal component analysis was performed,
748 and the first 50 PCAs were used to identify nearest neighbors, and interconnected clusters were
749 identified with a resolution of 0.35. UMAP was used to visualize the results. Preliminary
750 dimensionality reduction and visualization with UMAP using 50 PCAs identified a large microglia
751 cluster, plus clusters of other cell types. The non-proliferative microglia clusters were subsetted
752 for further analysis (the macrophage cluster was differentiated from the microglia cluster based
753 on increased expression of *Mcp1, Pf4,* and *Ms4a7*). The data was scaled and centered. Principal
754 component analysis was performed, and the first 10 PCAs were used for UMAP dimensionality
755 reduction and to identify nearest neighbors, and interconnected clusters were identified with a
756 resolution of 0.20.
757
758 Monocle 3: Monocle 3 was used to generate the pseudotime analysis[55-58]. Data was imported
759 from Seurat analysis and a Monocle dataset was generated. The dataset was preprocessed with
760 normalization of the data and PCA generation. Next, the preprocessed data underwent further
761 non-linear dimensionality reduction using UMAP. Cells were clustered, and trajectories were

762 determined for cells within a cluster. For determining “pseudotime” aging of microglia, the root
763 node of the pseudotime trajectory was manually placed in the cluster of 6-month cells. The graph
764 segments of the pseudotime trajectories resulting in inflammatory activation were chosen for
765 further analysis. Graph autocorrelation analysis was performed on the inflammatory trajectory
766 using Moran’s I, which determines if genes are expressed in focal regions of graph space. A cutoff
767 q-value of 0.005 was set as significant for focal expression. Subsequently, coregulated modules
768 were determined using Louvain community analysis at an optimized resolution of 0.0078. The
769 modules were then overlaid onto the UMAP plot to determine the region of the trajectory with focal
770 expression of the module. The ten most significant genes of each module, as determined by q-
771 value were used to construct the heatmaps in Figures 3F and 3I. The significant genes of each
772 module were used to determine the effects of manipulations in the presence of LPS in Figure 3J.
773

774 **Immunohistochemistry**

775 Mice were sedated with ketamine followed by perfusion with 30mL of ice-cold PBS. Brains were
776 collected from PBS perfused mice and fixed overnight at 4°C in 4% paraformaldehyde in PBS.
777 The brains were washed with PBS and immersed in 30% sucrose (in PBS), and then stored at
778 4°C until the brains sank. 40μM coronal sections were sliced using a microtome at -20°C. Sections
779 were stored in cryopreservation buffer (40% PB Buffer (0.02 M Sodium Phosphate Monobasic,
780 0.08 M Sodium Phosphate Dibasic, pH 7.4), 30% Glycerol, 30% Ethylene Glycol) at -20°C until
781 staining. Hippocampal sections were washed three times in TBST. Sections were permeabilized
782 in pretreatment buffer (0.1% Triton-X in TBST) with rocking for 1 hour at room temperature. After
783 three washes in TBST, sections were blocked in 5% goat serum for 2 hours (for IBA1/CD68
784 double stain) or 5% donkey serum (NFKB/Iba1 and C1q/C3/Iba1 stains). Blocking buffer was
785 replaced with primary antibody mixture and incubated overnight at 4°C with rocking. The following
786 primary antibodies were used: rabbit anti-IBA1 (1:1000, Wako, Cat# 019-19741,
787 RRID:AB_839504), rat anti-CD68 (1:250, Bio-Rad, Cat# MCA1957, RRID:AB_322219), rabbit
788 anti-NFKB p65 (1:500, Santa Cruz, Cat# sc-372, RRID:AB_632037), guinea pig anti-Iba1 (1:1000,
789 Synaptic Systems, Cat# 234-004, RRID:AB_2493179), rabbit anti-C1q (1:1000, Abcam, Cat#
790 ab182451, RRID:AB_2732849), rat anti-C3 (1:1000, Abcam, Cat# ab11862, RRID:AB_2066623),
791 and rabbit anti-S6 (1:500, Cell Signaling, Cat# 2217, RRID:AB_331355). The sections were
792 washed three times with TBST. Subsequently, secondary antibody solution was added to the
793 sections, and incubated at room temperature with rocking for two hours. The following secondary
794 antibodies were used: goat anti-rabbit AlexaFluor 488 (Life Technologies, Cat# A-11008,
795 RRID:AB_143165), goat anti-rat AlexaFluor 555 (Life Technologies, Cat# A-21434,

796 RRID:AB_2535855), donkey anti-guinea pig AlexaFluor 488 (Jackson Immuno, Cat# 706-545-
797 148, RRID:AB_2340472), donkey anti-rabbit AlexaFluor 555 (Life Technologies, Cat# A-31572,
798 RRID:AB_162543), and donkey anti-rat AlexaFluor 647 (Jackson Immuno, Cat# 712-606-150,
799 RRID:AB_2340695). The sections were washed three times with TBST, with the first wash
800 containing Hoescht 33342 (Invitrogen, H3570) at a concentration of 1μg/mL. The sections were
801 transferred to phosphate buffer and mounted on frosted slides. Coverslips were mounted with
802 Prolong Gold Antifade (Thermo Fisher, P10144) reagent after the sections were dried. Slides
803 were imaged at 20x magnification on a Zeiss LSM 800 or LSM900 for a final resolution of
804 0.312μM/pixel. 8-9 z-planes were imaged at 3μM intervals. The hippocampus was imaged, and
805 the tiled images were stitched together with Zeiss ZenPro software. 2-3 hippocampal sections
806 were imaged from each sample.
807
808 Images were analyzed with FIJI. Maximum intensity projections of Z-stacked images were
809 constructed. Images were converted to 8-bit images and consistent adjustments were made for
810 each channel within an experiment. The Iba1 channel was used to quantify microglia using the
811 particle counter function in FIJI and the counts were validated by manual visual counting. The
812 presence of CD68, NFKB(p65), C3, or C1q in microglia was determined by creating ROIs within
813 the microglia in a field using the create selection function on the Iba1 images. The ROIs of the
814 hippocampal subregions and the microglia were combined, and CD68 puncta meeting a minimum
815 particle size threshold (100 pixels, equating to 31.2μM) within microglia determined if the microglia
816 were activated (CD68+IBA1+), while the measure function determined the intensity of NFKB(p65),
817 C3, or C1q. To determine percent activation of microglia with IBA1/CD68 staining, we divided the
818 number of microglia that were activated (CD68+IBA1+) by the total number of microglia (IBA1+)
819 in the analyzed regions and multiplied by 100.
820
821 ***In vitro* treatment of microglia**
822 Mixed glial cultures were generated from p1 male pups. Cortices and hippocampi were isolated
823 from the pups, and meninges were removed. The tissue was broken up by repeatedly pipetting
824 up and down, followed by dissociation with Trypsin. Single cell suspensions were plated on poly-
825 L-lysine coated flasks in DMEM (Thermo Fisher, 11965-118) supplemented with 10% FBS
826 (Gemini Bio-Products, 900-208) and antibiotic mix (Penicillin/Streptomycin)(Genesee Scientific,
827 25-512) and incubated at 37°C in 5% CO_2. Media was changed after 4 days to remove debris.
828 Microglia were isolated after 14 days by agitating the plates to dislodge microglia, then transferring
829 the supernatant of each sample evenly amongst 4 wells of a 24 well plate. Microglia were

830 incubated for 16 hours followed by replacement with serum free macrophage SFM media (Thermo
831 Fisher, 12065074) supplemented with M-CSF (10ng/m) (Peprotech, 315-02) and antibiotic mix.
832 After 24 hours microglia were treated with RNA polymerase I Inhibitor 2, CX-5461 (100nM)(EMD
833 Millipore, 509265) or human TGFβ1 recombinant protein (10ng/mL)(ThermoFisher Scientific,
834 PHG9204) for 24 hours followed by addition of lipopolysaccharides (LPS, 200ng/uL) from *E. coli*
835 (Sigma-Aldrich, L2018) for 8 hours and ATP (10nM)(InvivoGen, tlrl-atpl) for 30 minutes. Tri
836 Reagent was added to the culture plate, and the plates were shaken for 5 minutes. RNA was
837 isolated according to manufacturer's instructions. RNA-Seq libraries were generated as above for
838 the bulk RNA-Seq.
839
840 **RNAscope**
841 RNAscope was performed with the RNAscope® Multiplex Fluorescent Reagent Kit v2 (ACD,
842 323110). 40μM coronal sections were washed with TBST, then incubated with hydrogen peroxide
843 for 45 minutes at 25°C. After washing with TBST, the sections were incubated in Target Retrieval
844 Buffer at 95°C for 10 minutes. The sections were mounted on slides and dried overnight. The
845 sections were treated with RNAscope Protease III for 10 minutes at 40°C. Sections were washed
846 in water four times. Sections were incubated with *Tgfb1* probe (ACD, 443571-C2) for 2 hours at
847 40°C. The sections were washed twice with RNAscope wash buffer. The sections were incubated
848 with AMP1 for 30 minutes, AMP2 for 30 minutes, AMP3 for 15 minutes, HRP-C2 for 15 minutes,
849 TSA Plus Cy3 (1:1000, Perkin Elmer, SKU NEL744001KT) for 30 minutes, and HRP-Blocker for
850 15 minutes; all at 40°C with washes with RNAscope wash buffer between every incubation. RNA-
851 Protein Co-Detection Ancillary Kit (ACD, 323180) buffer was used to block the sections before
852 incubating with rabbit anti-IBA1 (1:500, Wako, Cat# 019-19741, RRID:AB_839504) overnight at
853 4°C. Sections were washed three times in TBST. Sections were incubated with secondary
854 antibody solution with goat anti-rabbit AlexaFluor 488 (1:1000, Life Technologies, Cat# A-11008,
855 RRID:AB_143165) for two hours at room temperature. The sections were washed three times
856 with TBST, with the first wash containing Hoescht 33342 (Invitrogen, H3570) at a concentration
857 of 1μg/mL Coverslips were mounted with Prolong Gold Antifade (Thermo Fisher, P10144) reagent
858 after the sections were dried. Slides were imaged at 40x magnification on a Zeiss LSM 900. 10
859 z-planes were imaged at 1μM intervals.
860
861 Images were analyzed with FIJI. Maximum intensity projections of Z-stacked images were
862 constructed. Images were converted to 8-bit images and the *Tgfb1* was thresholded. For each

863 section, the intensity of 5-7 individual *Tgfb1* puncta were averaged to get the average puncta
864 intensity of that section. The intensity of all *Tgfb1* signal in clearly identifiable individual IBA1 cells
865 was measured for 20-25 cells in the molecular layer of the hippocampus. The mean *Tgfb1* count
866 per microglia for each sample was calculated by dividing the average *Tgfb1* intensity in IBA1 cells
867 by the average puncta intensity.
868
869 **Contextual fear conditioning**
870 In this task, mice learned to associate the environmental context (fear conditioning chamber) with
871 an aversive stimulus (mild foot shock; unconditioned stimulus, US) during the training phase
872 enabling testing for hippocampal- dependent contextual fear conditioning. To also assess
873 amygdala-dependent cued fear conditioning, the mild foot shock was paired with a light and tone
874 cue (conditioned stimulus, CS) during the training phase. Conditioned fear was displayed as
875 freezing behavior. Specific training parameters are as follows: tone duration is 30 seconds; level
876 is 70 dB, 2 kHz; shock duration is 2 seconds; intensity is 0.6 mA. This intensity is not painful and
877 can easily be tolerated but will generate an unpleasant feeling. More specifically, on day 1 each
878 mouse was placed in a fear-conditioning chamber and allowed to explore for 2 min before delivery
879 of a 30-second tone (70 dB) and light ending with a 2-second foot shock (0.6 mA). Two minutes
880 later, a second CS-US pair was delivered. On day 2, each mouse was first placed in the fear-
881 conditioning chamber containing the same exact context, but with no CS or foot shock. Freezing
882 was analyzed for 2 minutes and represented as the percentage of time that the mouse froze over
883 the 2 minutes. One hour later, the mice were placed in a new context containing a different odor,
884 floor texture, chamber walls and shape. Animals were allowed to explore for 2 minutes before
885 being re-exposed to the CS. Freezing was analyzed for 30 seconds following the CS and
886 represented as the percentage of time that the mouse froze over those 30 seconds. Determination
887 of freezing behavior was performed using FreezeScan video tracking system and software
888 (Cleversys, Inc). Single outliers were removed using the extreme studentized deviate method
889 (Grubbs' test) with an alpha of 0.05.
890
891 **Novel object recognition**
892 The novel object recognition task was adapted from a previously described protocol[59].
893 Specifically, during the habituation phase (day 1), mice could freely explore an empty open field
894 arena for 10 minutes (motor activity and anxiety (time in center) were measured during this
895 phase). During the training phase (day 2), two identical objects were placed in the habituated
896 arena, and mice could explore the objects for 5 minutes. For the testing phase (day 3), one object

897 was replaced with a novel object, and mice could explore the objects for 5 minutes. Time spent
898 exploring each object was quantified using the Smart Video Tracking Software (Panlab; Harvard
899 Apparatus). Two different sets of objects are used. To control for any inherent object preference,
900 half of the mice are exposed to object A as their novel object and half to object B. To control for
901 any potential object-independent location preference, the location of the novel object relative to
902 the trained object is also varied. The objects were chosen based on their ability to capture the
903 animal's interest, independent of genetic background or age. To determine percent time with
904 novel object, we calculate (Time with novel object)/(Time with Trained Object + Time with Novel
905 Object) * 100. In this preference index, 100% indicates full preference for the novel object, and
906 0% indicates full preference for the trained object. A mouse with a value of 50% would have spent
907 equal time exploring both objects. Mice that did not explore both objects for 5 seconds during the
908 training phase or testing phase were excluded from analysis. Single outliers were removed using
909 the extreme studentized deviate method (Grubbs' test) with an alpha of 0.05.
910
911 **Y maze**
912 The Y Maze task was conducted using an established forced alternation protocol[60]. During the
913 training phase, mice were placed in the start arm facing the wall and allowed to explore the start
914 and trained arm for 5 minutes, while entry to the 3rd arm (novel arm) was blocked. The maze was
915 cleaned between each mouse to remove odor cues, and the trained arm was alternated between
916 mice. The mouse was then removed to its home cage. After 30 minutes, the block was removed,
917 and the mouse was returned to the start arm and allowed to explore all 3 arms for 5 minutes. Time
918 spent in each arm was quantified using the Smart Video Tracking Software (Panlab; Harvard
919 Apparatus). The percent time in the novel arm was defined as time in the novel arm divided by
920 time spent in the novel and trained arms during the task.
921
922 **Datasets**
923 All RNA-Seq and scRNA-Seq data have been deposited in the Gene Expression Omnibus and
924 are publicly available as of the date of publication. The following datasets were generated for this
925 manuscript and deposited in Gene Expression Omnibus: aging single-cell RNA-Seq
926 (GSE179358), *in vitro* treated primary microglia (GSE179611), and *Tgfb1* cKO microglia RNA-
927 Seq (GSE190007).
928
929 **Statistics**

Researchers were blinded throughout histological assessments with groups being un-blinded at the end of each experiment upon statistical analysis. Data are expressed as mean ± s.e.m with individual sample values being shown. Statistical analysis was performed with Prism 8.0 (GraphPad), R, DESeq2, Seurat, or Monocle 3. Comparisons of means in histology experiments were analyzed with multiple T-tests followed by Holm-Sidak correction or mixed effects analysis followed by Dunnett's multiple comparisons (Prism). Changes in expression for aggregated gene sets were determined with one sample T-tests with the expected value of 0 in log2 space (null hypothesis of no change). Differential expression analysis in DESeq2 was based on Wald's significance test of the negative binomial distribution. Differential expression analysis of single-cell RNA-Seq data in Seurat was performed using non-parametric Wilcoxon rank sum tests. Autocorrelation analysis to determine focal expression Monocle 3 was done using Moran's I. The significance of gene set overlap was determined using the χ^2 test with R. All data generated or analyzed in this study are included in this article.

964 **SUPPLEMENTAL MATERIAL**

965

966 **Fig. S1 | Hippocampal microglia exhibit age-related heterogeneity during aging. A,** UMAP
967 plot of all Cd11b+ cells. Several adjacent clusters of microglia were identified, as well as a cluster
968 of proliferating microglia. Smaller populations of peripheral immune cell types – macrophages and
969 neutrophils – were identified. Clusters of astrocytes and vascular cells were also found. Overall,
970 greater than 82% of cells were microglia. (n = 1 pool of 5 animals for each age) **B,** Dot plot showing
971 expression (average expression and percent of cells expressing) of top two markers for each
972 cluster. **C,** UMAP plots with expression levels of microglia markers superimposed onto cells.
973 Notice that peripheral immune cells express microglia markers; however, they are distinguished
974 from microglia based on marker expression from (b). **D-G,** Volcano plots of differential gene
975 expression for the clusters identified in Figure 1A compared to every other cluster for Homeostatic
976 (**D**), Transition (**E**), Activation (**F**), and Interferon (**G**) microglia clusters. **H,** Cluster composition of
977 non-proliferating microglia by age. **I,** Standardized variation of non-proliferating microglia for each
978 age. **J,** Representative images of NFκB (p65) (yellow) and IBA1 (cyan) staining in the
979 hippocampus of 3- and 24-month-old mice and quantification of staining in 3-, 6-, 12-, 18-, and
980 24-month-old mice. (n=5 mice per group; one-way ANOVA with Dunnett's post hoc test; *P<0.05,
981 ***P<0.001)**.** **K,** Representative images of CD68 (red) and IBA1 (cyan) staining in the
982 hippocampus of 3- and 24-month-old mice and quantification of staining in 3-, 6-, 12-, 18-, and
983 24-month-old mice. (n=4-5 mice per group; one-way ANOVA with Dunnett's post hoc test;
984 *P<0.05, **P<0.01)**.** Data are shown as mean±s.e.m.

985
986
987
988
989
990
991
992
993
994
995
996
997

998 **Figure S2 | Hippocampal microglia aging advances through intermediate states that**
999 **respond to systemic interventions or disease states**. **A**, Volcano plot of differential gene
1000 expression of 12-month microglia versus all other ages with significant genes in teal. **B**, Gene
1001 ontology analysis of biological processes enriched in those genes with increased expression at
1002 12-months of age. **C**, Representative images and quantification of CD68 (red) and IBA1 (cyan)
1003 staining in the hippocampus of isochronic young (IY) and heterochronic young (HY) along with a
1004 diagram of the comparisons. (n=5 mice per group; unpaired Student's T-test; ***P<0.001)**.** Data
1005 are shown as mean±s.e.m. **D,** Dotplot of pseudotime modules in young (Y), isochronic young (IY),
1006 and heterochronic young (HY) parabiont microglia. Data is from Palovics *et al*[61]. Percent of cells
1007 expressing the gene and average normalized expression are represented. **E,** Volcano plots of
1008 differential gene expression of $App^{NL\text{-}G\text{-}F}$ genotype (AD) over wildtype (WT) microglia at 6- (left)
1009 and 12-months of age. Significant genes are in teal. Data is from Frigerio[62]. **F,** Dotplot of
1010 pseudotime modules across ages (3-, 6-, 12-, and 21-months old) and genotypes ($App^{NL\text{-}G\text{-}F}$
1011 genotype (AD) over C57Bl/6 (WT)). Data is from Frigerio[17]. Percent of cells expressing the gene
1012 and average normalized expression are represented.
1013
1014
1015
1016
1017
1018
1019
1020
1021
1022
1023
1024
1025
1026
1027
1028
1029
1030
1031

Fig. S3 | Intermediate states of microglia aging act as checkpoints on inflammatory progression. A, Quantification of percentage of *Tgfb1* RNAscope signal within IBA1 cells. **B**, Quantification of IHC of pTGFBR1 signal in IBA1 cells across ages. (n=4-5 mice per group; one-way ANOVA; *P<0.05) **C,** Dotplot of the expression values of TGFB1 signaling components from scRNA-Seq of aging hippocampal microglia (6-, 12-, 18-, and 24-month-old). Percent of cells expressing the gene and average normalized expression are represented. **D**, Dotplot of the expression values of TGFB1 signaling components in young (Y), aged (A), isochronic young (IY), and heterochronic young (HY) parabiont microglia. Data is from Palovics *et al*[61]. Percent of cells expressing the gene and average normalized expression are represented. UMAP plot of *Tgfb1* scRNA-Seq colored by genotype. **E**, Heatmap of gene expression changes in the top 10 genes in each aging module induced by LPS. **F**, Overlap between microglia gene expression changes induced by LPS and aging. (χ^2<2.2e-16). **G**, PCA plot of pharmacological manipulations with or without LPS treatment.

Fig. S4 | Targeting age-related changes in microglia-derived TGFB1 promotes microglia advancement along inflammatory trajectories in the hippocampus and impairs cognition. **A**, Representative images and quantification of IBA1 (cyan)/CD68 (red)-positive microglia in wildtype, *Tgfb1* cHet, and *Tgfb1* cKO hippocampi. (n=3-5; one way ANOVA with Tukey post hoc test; *P<0.05) **B,** Dotplot of the expression values of TGFB1 signaling components from scRNA-Seq of *Tgfb1* WT, cHet, and cKO microglia. (n = 2 pools of 3 animals per genotype) **C,** UMAP plot of *Tgfb1* scRNA-Seq colored by genotype. **D,** FACS plots of gating strategy for microglia isolation for RNA-Seq in cHet and cKO hippocampi. Quantification of the flow cytometry analysis of CD11b and CD45. (n=3-5; mixed effects analysis; *P<0.05, ****P<0.0001). **E**, Example histogram and quantification of CD48 in control and *Tgfb1* cKO FACS-sorted microglia. (n=3-5 per group; T-test; ****P<0.0001). **F,** Top gene ontology terms associated with genes significantly increased in microglia bulk RNA-Seq in *Tgfb1* cKO samples (n=3-5 samples per genotype). **G**, Top gene ontology terms associated with genes significantly decreased in microglia bulk RNA-Seq in *Tgfb1* cKO samples. **H**, Overlap between concordant microglia gene expression changes induced by *Tgfb1* knockout and aging. (χ^2<2.2e-16). **I**, Heatmap of gene expression of the top 10 genes in each aging module in control and *Tgfb1* cKO microglia. **J**, Average gene expression changes for each aging module represented as log2 fold change of *Tgfb1* cKO over control. (one sample T-test with the expected value of 0 (no change); ****P<0.0001). **K**, Freezing during the cued fear conditioning phase of the fear conditioning test. The percent freezing was calculated for the last 30 seconds of the test following the conditioned stimulus. (n=13-16 per genotype) **L**, Diagram and results of Y-maze test. Results are presented as preference for the novel arm versus the trained armed (time in novel arm/ (time in novel arm + trained arm) x 100). (n=14-16 per genotype) **M**, Percent time in the center of the open field and distance traveled during the open field test. (n=14-16 per genotype) Data are shown as mean±s.e.m.

Table S1 | Gene markers for each age group and differential expression between the 6- and 12-, 18-, or 24-month-old microglia in single-cell RNA-Seq of aging hippocampal microglia. The tables contain genes selectively increased or decreased in each age group when compared to every other age group combined and genes differentially expressed between 6- and 12-, 18-, or 24-month microglia. The tables contain the average log fold change, the percentage of cells in each group with expression, and the adjusted p-value.

Table S2 | Pseudotime trajectories of aging microglia. The pseudotime analysis contains the spatial autocorrelation analysis. Moran's I was used to detect focal expression of genes that were consequently constructed into co-regulated modules using Louvain community analysis. The table contains the adjusted p-value (q-value) and module information.

Table S3 | RNA-Seq analysis of primary microglia treated with LPS and TGFB1 or CX-5461. The tables contain the RNA-Seq differential expression analysis of control and LPS activated primary microglia, DMSO and CX-5461 treated primary microglia activated by LPS, and DMSO and TGFB1 treated primary microglia activated by LPS, respectively. The tables contain expression values of genes for the samples that were compared along with mean expression values for all samples combined, log fold change between sample groups, and adjusted p-values. in the RNA-Seq differential expression analysis of control and LPS activated primary microglia, DMSO and CX-5461 treated primary microglia activated by LPS, and DMSO and TGFB1 treated primary microglia activated by LPS, respectively.

Table S4 | Differential expression analysis of control and *Tgfb1* cKO hippocampal microglia. The table contains expression values of genes for the samples that were compared along with mean expression values for all samples combined, log fold change between sample groups, and adjusted p-values.

1233 **REFERENCES**

1234

1235 1 Waisman, A., Ginhoux, F., Greter, M. & Bruttger, J. Homeostasis of Microglia in the Adult
1236 Brain: Review of Novel Microglia Depletion Systems. *Trends in immunology* **36**, 625-636,
1237 doi:10.1016/j.it.2015.08.005 (2015).

1238 2 Salter, M. W. & Beggs, S. Sublime microglia: expanding roles for the guardians of the
1239 CNS. *Cell* **158**, 15-24, doi:10.1016/j.cell.2014.06.008 (2014).

1240 3 Mosher, K. I. & Wyss-Coray, T. Microglial dysfunction in brain aging and Alzheimer's
1241 disease. *Biochem Pharmacol* **88**, 594-604, doi:10.1016/j.bcp.2014.01.008 (2014).

1242 4 Bachiller, S. *et al.* Microglia in Neurological Diseases: A Road Map to Brain-Disease
1243 Dependent-Inflammatory Response. *Front Cell Neurosci* **12**, 488,
1244 doi:10.3389/fncel.2018.00488 (2018).

1245 5 Sierra, A., Gottfried-Blackmore, A. C., McEwen, B. S. & Bulloch, K. Microglia derived from
1246 aging mice exhibit an altered inflammatory profile. *Glia* **55**, 412-424,
1247 doi:10.1002/glia.20468 (2007).

1248 6 Marschallinger, J. *et al.* Lipid-droplet-accumulating microglia represent a dysfunctional
1249 and proinflammatory state in the aging brain. *Nature neuroscience* **23**, 194-208,
1250 doi:10.1038/s41593-019-0566-1 (2020).

1251 7 Pluvinage, J. V. *et al.* CD22 blockade restores homeostatic microglial phagocytosis in
1252 ageing brains. *Nature*, doi:10.1038/s41586-019-1088-4 (2019).

1253 8 Damani, M. R. *et al.* Age-related alterations in the dynamic behavior of microglia. *Aging*
1254 *Cell* **10**, 263-276, doi:10.1111/j.1474-9726.2010.00660.x (2011).

1255 9 Flanary, B. E., Sammons, N. W., Nguyen, C., Walker, D. & Streit, W. J. Evidence that
1256 aging and amyloid promote microglial cell senescence. *Rejuvenation Res* **10**, 61-74,
1257 doi:10.1089/rej.2006.9096 (2007).

1258 10 Udeochu, J. C., Shea, J. M. & Villeda, S. A. Microglia communication: Parallels between
1259 aging and Alzheimer's disease. *Clin Exp Neuroimmunol* **7**, 114-125,
1260 doi:10.1111/cen3.12307 (2016).

1261 11 Grabert, K. *et al.* Microglial brain region-dependent diversity and selective regional
1262 sensitivities to aging. *Nature neuroscience* **19**, 504-516, doi:10.1038/nn.4222 (2016).

1263 12 Burns, J. C. *et al.* Differential accumulation of storage bodies with aging defines discrete
1264 subsets of microglia in the healthy brain. *Elife* **9**, doi:10.7554/eLife.57495 (2020).

1265 13 Hammond, T. R. *et al.* Single-Cell RNA Sequencing of Microglia throughout the Mouse
1266 Lifespan and in the Injured Brain Reveals Complex Cell-State Changes. *Immunity* **50**, 253-
1267 271 e256, doi:10.1016/j.immuni.2018.11.004 (2019).

1268 14 Li, X. *et al.* Transcriptional and epigenetic decoding of the microglial aging process. *Nat*
1269 *Aging* **3**, 1288-1311, doi:10.1038/s43587-023-00479-x (2023).

15 Silvin, A. *et al.* Dual ontogeny of disease-associated microglia and disease inflammatory macrophages in aging and neurodegeneration. *Immunity* **55**, 1448-1465 e1446, doi:10.1016/j.immuni.2022.07.004 (2022).

16 Keren-Shaul, H. *et al.* A Unique Microglia Type Associated with Restricting Development of Alzheimer's Disease. *Cell* **169**, 1276-1290 e1217, doi:10.1016/j.cell.2017.05.018 (2017).

17 Sala Frigerio, C. *et al.* The Major Risk Factors for Alzheimer's Disease: Age, Sex, and Genes Modulate the Microglia Response to Abeta Plaques. *Cell Rep* **27**, 1293-1306 e1296, doi:10.1016/j.celrep.2019.03.099 (2019).

18 Lee, S. *et al.* APOE modulates microglial immunometabolism in response to age, amyloid pathology, and inflammatory challenge. *Cell Rep* **42**, 112196, doi:10.1016/j.celrep.2023.112196 (2023).

19 Masuda, T. *et al.* Spatial and temporal heterogeneity of mouse and human microglia at single-cell resolution. *Nature* **566**, 388-392, doi:10.1038/s41586-019-0924-x (2019).

20 Kaya, T. *et al.* CD8(+) T cells induce interferon-responsive oligodendrocytes and microglia in white matter aging. *Nature neuroscience* **25**, 1446-1457, doi:10.1038/s41593-022-01183-6 (2022).

21 Yousef, H. *et al.* Aged blood impairs hippocampal neural precursor activity and activates microglia via brain endothelial cell VCAM1. *Nat Med* **25**, 988-1000, doi:10.1038/s41591-019-0440-4 (2019).

22 Rebo, J. *et al.* A single heterochronic blood exchange reveals rapid inhibition of multiple tissues by old blood. *Nat Commun* **7**, 13363, doi:10.1038/ncomms13363 (2016).

23 Villeda, S. A. *et al.* The ageing systemic milieu negatively regulates neurogenesis and cognitive function. *Nature* **477**, 90-94, doi:10.1038/nature10357 (2011).

24 Li, Q. *et al.* Developmental Heterogeneity of Microglia and Brain Myeloid Cells Revealed by Deep Single-Cell RNA Sequencing. *Neuron* **101**, 207-223 e210, doi:10.1016/j.neuron.2018.12.006 (2019).

25 Kracht, L. *et al.* Human fetal microglia acquire homeostatic immune-sensing properties early in development. *Science (New York, N.Y.)* **369**, 530-537, doi:10.1126/science.aba5906 (2020).

26 Fan, X., Wheatley, E. G. & Villeda, S. A. Mechanisms of Hippocampal Aging and the Potential for Rejuvenation. *Annu Rev Neurosci* **40**, 251-272, doi:10.1146/annurev-neuro-072116-031357 (2017).

27 Millet, A., Ledo, J. H. & Tavazoie, S. F. An exhausted-like microglial population accumulates in aged and APOE4 genotype Alzheimer's brains. *Immunity* **57**, 153-170 e156, doi:10.1016/j.immuni.2023.12.001 (2024).

28 Harrington, E. P. *et al.* MHC class I and MHC class II reporter mice enable analysis of immune oligodendroglia in mouse models of multiple sclerosis. *Elife* **12**, doi:10.7554/eLife.82938 (2023).

29 Shi, Q. *et al.* Complement C3-Deficient Mice Fail to Display Age-Related Hippocampal Decline. *J Neurosci* **35**, 13029-13042, doi:10.1523/jneurosci.1698-15.2015 (2015).

30 Butovsky, O. *et al.* Identification of a unique TGF-beta-dependent molecular and functional signature in microglia. *Nature neuroscience* **17**, 131-143, doi:10.1038/nn.3599 (2014).

31 Pálovics, R. *et al.* Molecular hallmarks of heterochronic parabiosis at single-cell resolution. *Nature* **603**, 309-314, doi:10.1038/s41586-022-04461-2 (2022).

32 Yi, Y. W., You, K. S., Park, J. S., Lee, S. G. & Seong, Y. S. Ribosomal Protein S6: A Potential Therapeutic Target against Cancer? *Int J Mol Sci* **23**, doi:10.3390/ijms23010048 (2021).

33 Spittau, B., Dokalis, N. & Prinz, M. The Role of TGFbeta Signaling in Microglia Maturation and Activation. *Trends in immunology* **41**, 836-848, doi:10.1016/j.it.2020.07.003 (2020).

34 Cserép, C., Pósfai, B. & Dénes, Á. Shaping Neuronal Fate: Functional Heterogeneity of Direct Microglia-Neuron Interactions. *Neuron* **109**, 222-240, doi:10.1016/j.neuron.2020.11.007 (2021).

35 Horowitz, A. M. *et al.* Blood factors transfer beneficial effects of exercise on neurogenesis and cognition to the aged brain. *Science (New York, N.Y.)* **369**, 167-173, doi:10.1126/science.aaw2622 (2020).

36 Traschütz, A., Kummer, M. P., Schwartz, S. & Heneka, M. T. Variability and temporal dynamics of novel object recognition in aging male C57BL/6 mice. *Behav Processes* **157**, 711-716, doi:10.1016/j.beproc.2017.11.009 (2018).

37 Phillips, R. G. & LeDoux, J. E. Differential contribution of amygdala and hippocampus to cued and contextual fear conditioning. *Behav Neurosci* **106**, 274-285, doi:10.1037//0735-7044.106.2.274 (1992).

38 Kraeuter, A. K., Guest, P. C. & Sarnyai, Z. The Y-Maze for Assessment of Spatial Working and Reference Memory in Mice. *Methods Mol Biol* **1916**, 105-111, doi:10.1007/978-1-4939-8994-2_10 (2019).

39 Wek, R. C. Role of eIF2alpha Kinases in Translational Control and Adaptation to Cellular Stress. *Cold Spring Harb Perspect Biol* **10**, doi:10.1101/cshperspect.a032870 (2018).

40 Lopez-Otin, C., Blasco, M. A., Partridge, L., Serrano, M. & Kroemer, G. The hallmarks of aging. *Cell* **153**, 1194-1217, doi:10.1016/j.cell.2013.05.039 (2013).

41 Chovatiya, R. & Medzhitov, R. Stress, inflammation, and defense of homeostasis. *Mol Cell* **54**, 281-288, doi:10.1016/j.molcel.2014.03.030 (2014).

42 Xu, Z. X. *et al.* Elevated protein synthesis in microglia causes autism-like synaptic and behavioral aberrations. *Nat Commun* **11**, 1797, doi:10.1038/s41467-020-15530-3 (2020).

43 Yin, Z. *et al.* APOE4 impairs the microglial response in Alzheimer's disease by inducing TGFbeta-mediated checkpoints. *Nat Immunol* **24**, 1839-1853, doi:10.1038/s41590-023-01627-6 (2023).

44 Sarlus, H. & Heneka, M. T. Microglia in Alzheimer's disease. *J Clin Invest* **127**, 3240-3249, doi:10.1172/JCI90606 (2017).

45 Smith, L. K. *et al.* beta2-microglobulin is a systemic pro-aging factor that impairs cognitive function and neurogenesis. *Nat Med* **21**, 932-937, doi:10.1038/nm.3898 (2015).

46 Trombetta, J. J. *et al.* Preparation of Single-Cell RNA-Seq Libraries for Next Generation Sequencing. *Curr Protoc Mol Biol* **107**, 4 22 21-17, doi:10.1002/0471142727.mb0422s107 (2014).

47 Bray, N. L., Pimentel, H., Melsted, P. & Pachter, L. Near-optimal probabilistic RNA-seq quantification. *Nat Biotechnol* **34**, 525-527, doi:10.1038/nbt.3519 (2016).

48 Love, M. I., Huber, W. & Anders, S. Moderated estimation of fold change and dispersion for RNA-seq data with DESeq2. *Genome Biol* **15**, 550, doi:10.1186/s13059-014-0550-8 (2014).

49 Ashburner, M. *et al.* Gene ontology: tool for the unification of biology. The Gene Ontology Consortium. *Nat Genet* **25**, 25-29, doi:10.1038/75556 (2000).

50 Gene Ontology, C. The Gene Ontology resource: enriching a GOld mine. *Nucleic Acids Res* **49**, D325-D334, doi:10.1093/nar/gkaa1113 (2021).

51 Mi, H., Muruganujan, A., Ebert, D., Huang, X. & Thomas, P. D. PANTHER version 14: more genomes, a new PANTHER GO-slim and improvements in enrichment analysis tools. *Nucleic Acids Res* **47**, D419-D426, doi:10.1093/nar/gky1038 (2019).

52 Zheng, G. X. *et al.* Massively parallel digital transcriptional profiling of single cells. *Nat Commun* **8**, 14049, doi:10.1038/ncomms14049 (2017).

53 Marsh, S. E. *et al.* Dissection of artifactual and confounding glial signatures by single-cell sequencing of mouse and human brain. *Nat Neurosci* **25**, 306-316, doi:10.1038/s41593-022-01022-8 (2022).

54 Butler, A., Hoffman, P., Smibert, P., Papalexi, E. & Satija, R. Integrating single-cell transcriptomic data across different conditions, technologies, and species. *Nat Biotechnol* **36**, 411-420, doi:10.1038/nbt.4096 (2018).

55 Qiu, X. *et al.* Single-cell mRNA quantification and differential analysis with Census. *Nat Methods* **14**, 309-315, doi:10.1038/nmeth.4150 (2017).

56 Qiu, X. *et al.* Reversed graph embedding resolves complex single-cell trajectories. *Nat Methods* **14**, 979-982, doi:10.1038/nmeth.4402 (2017).

57 Trapnell, C. *et al.* The dynamics and regulators of cell fate decisions are revealed by pseudotemporal ordering of single cells. *Nat Biotechnol* **32**, 381-386, doi:10.1038/nbt.2859 (2014).

58 Cao, J. *et al.* The single-cell transcriptional landscape of mammalian organogenesis. *Nature* **566**, 496-502, doi:10.1038/s41586-019-0969-x (2019).

59 Leger, M. *et al.* Object recognition test in mice. *Nat Protoc* **8**, 2531-2537, doi:10.1038/nprot.2013.155 (2013).

60 Belarbi, K. *et al.* Beneficial effects of exercise in a transgenic mouse model of Alzheimer's disease-like Tau pathology. *Neurobiol Dis* **43**, 486-494, doi:10.1016/j.nbd.2011.04.022 (2011).

61 Palovics, R. *et al.* Molecular hallmarks of heterochronic parabiosis at single-cell resolution. *Nature* **603**, 309-314, doi:10.1038/s41586-022-04461-2 (2022).

62 Pasciuto, E. *et al.* Microglia Require CD4 T Cells to Complete the Fetal-to-Adult Transition. *Cell* **182**, 625-640 e624, doi:10.1016/j.cell.2020.06.026 (2020).

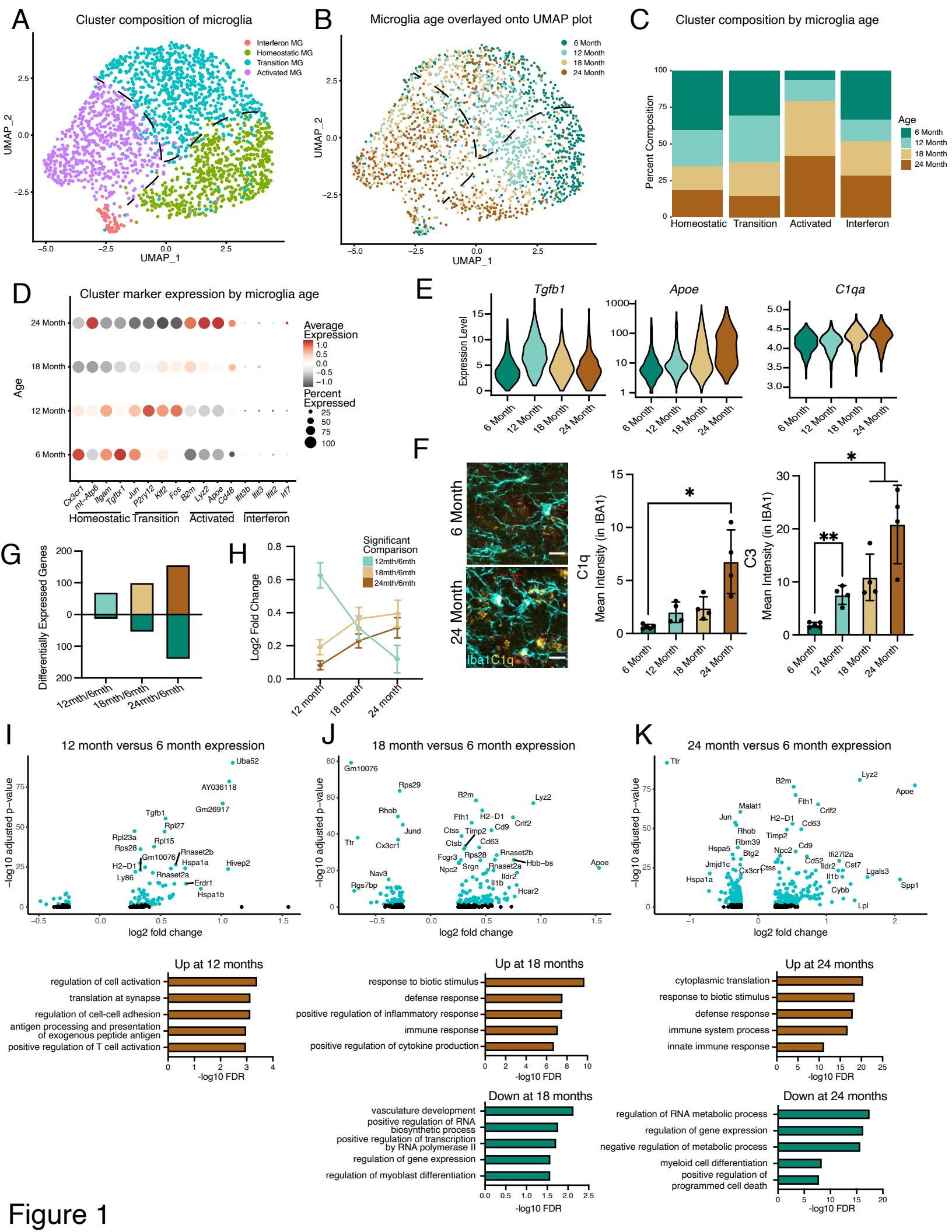
A
Cluster composition of microglia
Interferon MG
Homeostatic MG
Transition MG
Activated MG
UMAP_2
UMAP_1
B
Microglia age overlayed onto UMAP plot
6 Month
12 Month
18 Month
24 Month
C
Cluster composition by microglia age
Percent Composition
Homeostatic
Transition
Activated
Interferon
Age
D
Cluster marker expression by microglia age
Average Expression
Percent Expressed
Age
Cx3cr1
mt-Atp6
Itgam
Tgfbr1
Jun
P2ry12
Klf2
Fos
B2m
Lyz2
Apoe
Cd48
Ifit3b
Ifit3
Ifit2
Irf7
Homeostatic
Transition
Activated
Interferon
E
Tgfb1
Apoe
C1qa
Expression Level
F
6 Month
24 Month
Iba1C1qC3
C1q
C3
Mean Intensity (in IBA1)
G
Differentially Expressed Genes
12mth/6mth
18mth/6mth
24mth/6mth
H
Log2 Fold Change
Significant Comparison
12mth/6mth
18mth/6mth
24mth/6mth
I
12 month versus 6 month expression
J
18 month versus 6 month expression
K
24 month versus 6 month expression
−log10 adjusted p−value
log2 fold change
Up at 12 months
regulation of cell activation
translation at synapse
regulation of cell-cell adhesion
antigen processing and presentation of exogenous peptide antigen
positive regulation of T cell activation
Up at 18 months
response to biotic stimulus
defense response
positive regulation of inflammatory response
immune response
positive regulation of cytokine production
Up at 24 months
cytoplasmic translation
response to biotic stimulus
defense response
immune system process
innate immune response
Down at 18 months
vasculature development
positive regulation of RNA biosynthetic process
positive regulation of transcription by RNA polymerase II
regulation of gene expression
regulation of myoblast differentiation
Down at 24 months
regulation of RNA metabolic process
regulation of gene expression
negative regulation of metabolic process
myeloid cell differentiation
positive regulation of programmed cell death
-log10 FDR

Figure 1

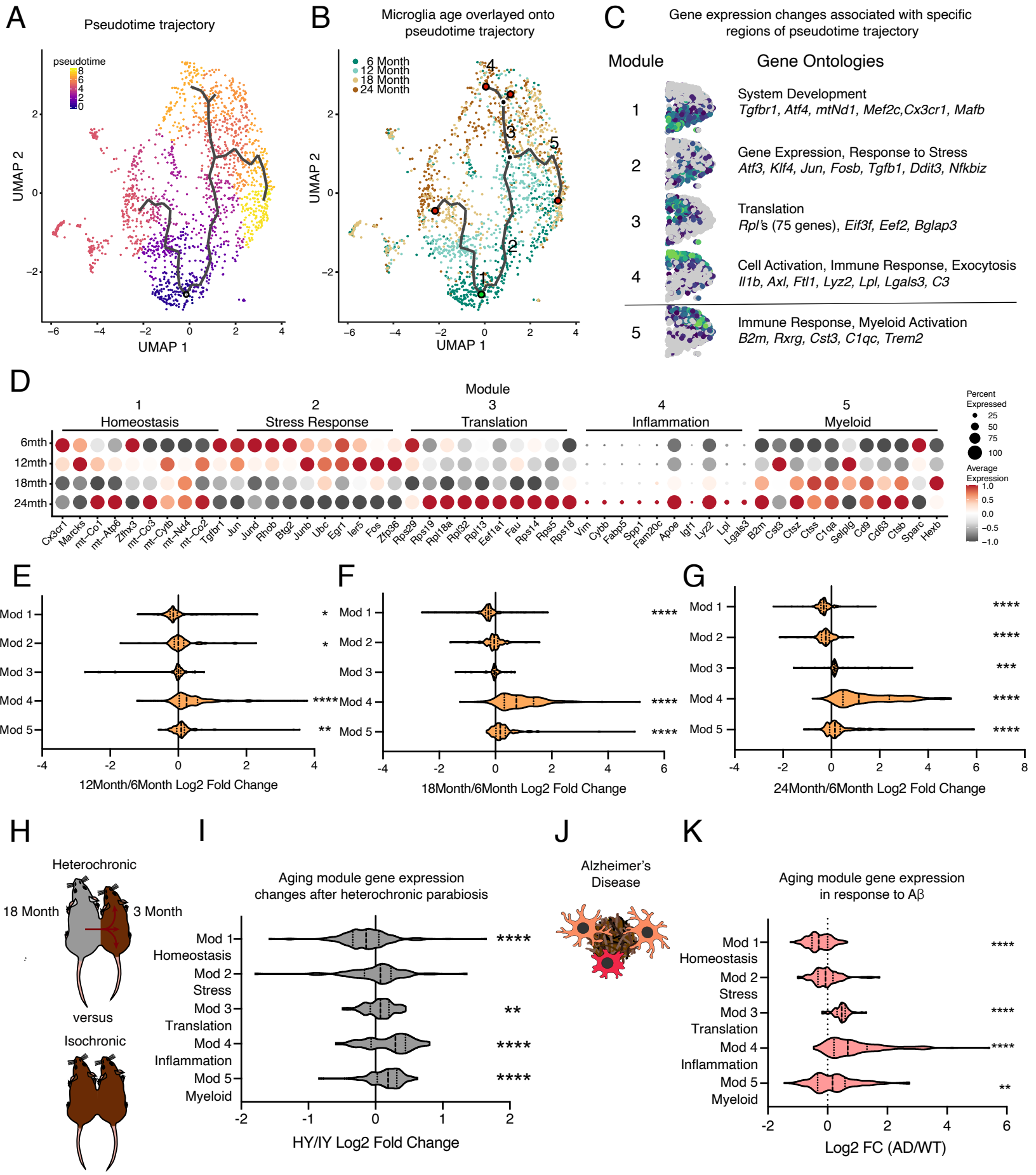
A
Pseudotime trajectory
pseudotime
UMAP 2
UMAP 1
B
Microglia age overlayed onto pseudotime trajectory
6 Month
12 Month
18 Month
24 Month
C
Gene expression changes associated with specific regions of pseudotime trajectory
Module
Gene Ontologies
1 System Development
Tgfbr1, Atf4, mtNd1, Mef2c,Cx3cr1, Mafb
2 Gene Expression, Response to Stress
Atf3, Klf4, Jun, Fosb, Tgfb1, Ddit3, Nfkbiz
3 Translation
Rpl's (75 genes), Eif3f, Eef2, Bglap3
4 Cell Activation, Immune Response, Exocytosis
Il1b, Axl, Ftl1, Lyz2, Lpl, Lgals3, C3
5 Immune Response, Myeloid Activation
B2m, Rxrg, Cst3, C1qc, Trem2
D
Module
1 Homeostasis
2 Stress Response
3 Translation
4 Inflammation
5 Myeloid
6mth
12mth
18mth
24mth
Percent Expressed
Average Expression
E
12Month/6Month Log2 Fold Change
F
18Month/6Month Log2 Fold Change
G
24Month/6Month Log2 Fold Change
H
Heterochronic
18 Month
3 Month
versus
Isochronic
I
Aging module gene expression changes after heterochronic parabiosis
Mod 1 Homeostasis
Mod 2 Stress
Mod 3 Translation
Mod 4 Inflammation
Mod 5 Myeloid
HY/IY Log2 Fold Change
J
Alzheimer's Disease
K
Aging module gene expression in response to Aβ
Log2 FC (AD/WT)

Figure 2

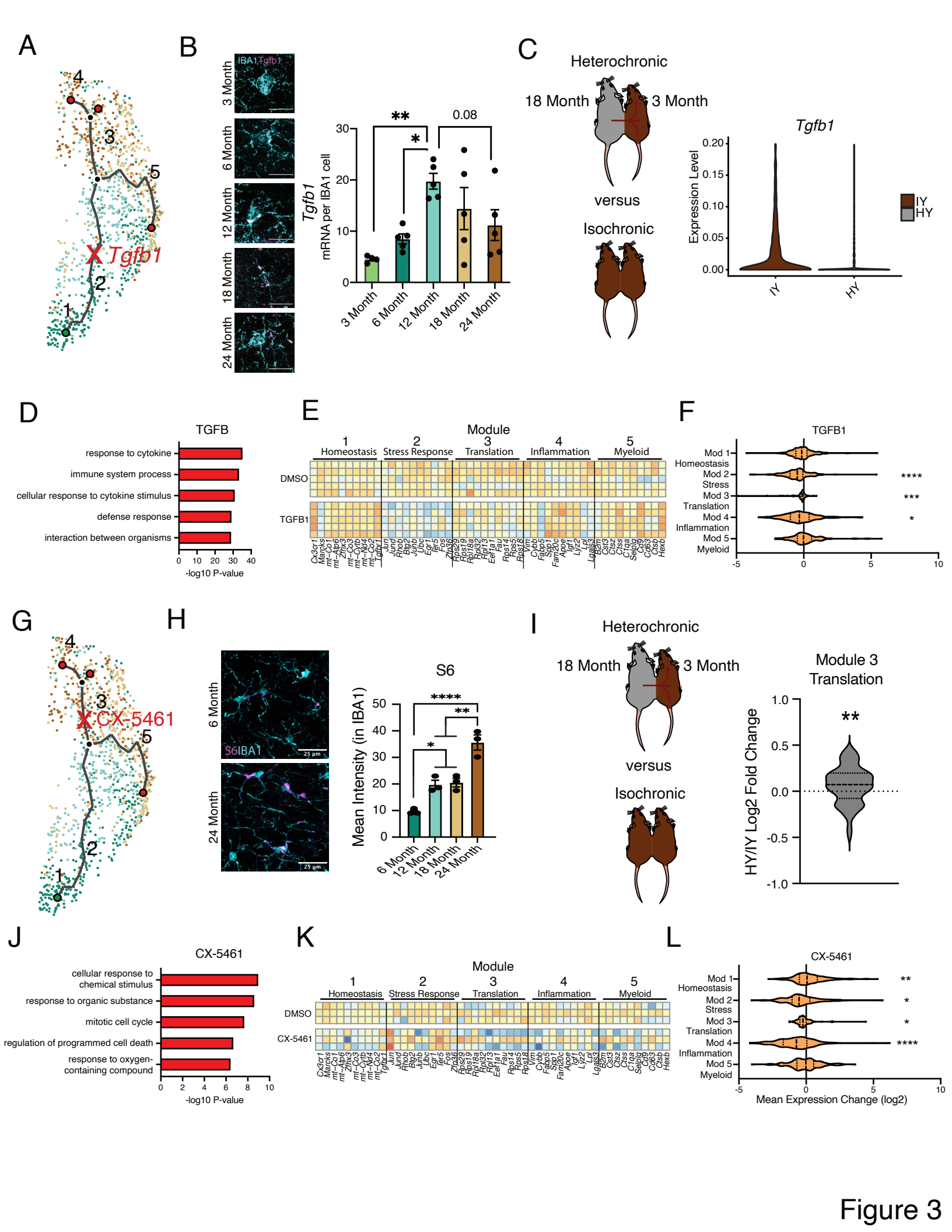
A
4
3
5
Tgfb1
2
1
B
IBA1,Tgfb1
3 Month
6 Month
12 Month
18 Month
24 Month
Tgfb1
mRNA per IBA1 cell
**
*
0.08
30
20
10
0
3 Month
6 Month
12 Month
18 Month
24 Month
C
Heterochronic
18 Month
3 Month
versus
Isochronic
Tgfb1
Expression Level
0.20
0.15
0.10
0.05
0.00
IY
HY
D
TGFB
response to cytokine
immune system process
cellular response to cytokine stimulus
defense response
interaction between organisms
0
10
20
30
40
-log10 P-value
E
Module
1
Homeostasis
2
Stress Response
3
Translation
4
Inflammation
5
Myeloid
DMSO
TGFB1
Cx3cr1
Marcks
mt-Co1
mt-Atp6
mt-Co3
Zfhx3
mt-Cytb
mt-Nd4
mt-Co2
Tgfb1
Jun
Jund
Rhob
Btg2
Junb
Ubc
Egr1
Ier5
Fos
Ztp36
Rps29
Rps19
Rpl18a
Rpl32
Rpl13
Eef1a1
Fau
Rps14
Rps5
Rps18
Vim
Cybb
Fabp5
Spp1
Fam20c
Apoe
Igf1
Lyz2
Lpl
Lgals3
B2m
Cst3
Ctsz
Ctss
C1qa
Selplg
Cd9
Cd63
Ctsb
Hexb
F
TGFB1
Mod 1
Homeostasis
Mod 2
Stress
Mod 3
Translation
Mod 4
Inflammation
Mod 5
Myeloid
****
***
*
-5
0
5
10
G
4
3
CX-5461
5
2
1
H
6 Month
24 Month
S6IBA1
25 µm
S6
Mean Intensity (in IBA1)
****
**
*
50
40
30
20
10
0
6 Month
12 Month
18 Month
24 Month
I
Heterochronic
18 Month
3 Month
versus
Isochronic
Module 3
Translation
HY/IY Log2 Fold Change
**
1.0
0.5
0.0
-0.5
-1.0
J
CX-5461
cellular response to chemical stimulus
response to organic substance
mitotic cell cycle
regulation of programmed cell death
response to oxygen-containing compound
0
2
4
6
8
10
-log10 P-value
K
Module
1
Homeostasis
2
Stress Response
3
Translation
4
Inflammation
5
Myeloid
DMSO
CX-5461
L
CX-5461
Mod 1
Homeostasis
Mod 2
Stress
Mod 3
Translation
Mod 4
Inflammation
Mod 5
Myeloid
**
*
*
****
-5
0
5
10
Mean Expression Change (log2)

Figure 3

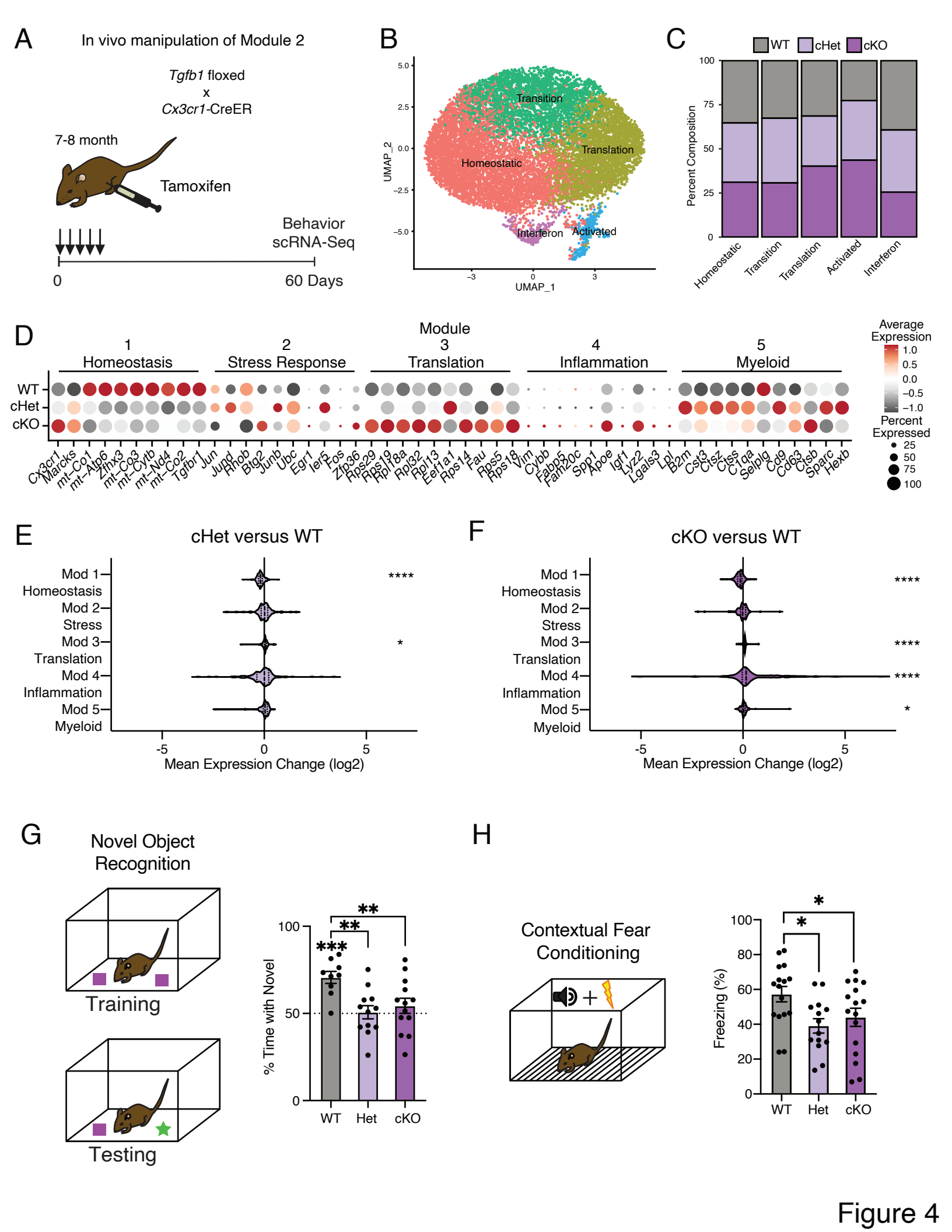
A
In vivo manipulation of Module 2
Tgfb1 floxed
x
Cx3cr1-CreER
7-8 month
Tamoxifen
Behavior
scRNA-Seq
0
60 Days
B
Transition
Translation
Homeostatic
Interferon
Activated
UMAP_1
UMAP_2
C
WT
cHet
cKO
Percent Composition
Homeostatic
Transition
Translation
Activated
Interferon
D
Module
1
Homeostasis
2
Stress Response
3
Translation
4
Inflammation
5
Myeloid
WT
cHet
cKO
Average Expression
Percent Expressed
E
cHet versus WT
Mod 1
Homeostasis
Mod 2
Stress
Mod 3
Translation
Mod 4
Inflammation
Mod 5
Myeloid
Mean Expression Change (log2)
F
cKO versus WT
Mean Expression Change (log2)
G
Novel Object
Recognition
Training
Testing
% Time with Novel
WT
Het
cKO
H
Contextual Fear
Conditioning
Freezing (%)
WT
Het
cKO

Figure 4